Sidewall Adhesion and Sliding Contact Behavior of Polycrystalline Silicon Microdevices Operated in High Vacuum

Daan Hein Alsem, Hua Xiang, Robert O. Ritchie, and Kyriakos Komvopoulos

***Abstract*—The reliability and performance of contact-mode microelectromechanical systems (MEMS) depend strongly on the tribological properties of contact interfaces. Knowledge of the dominant friction and wear mechanisms at submicrometer length scales is therefore of paramount importance to the design of MEMS devices with contact interfaces. The objective of this study was to examine changes in the adhesion behavior and morphology of sliding sidewall surfaces of polycrystalline silicon MEMS devices operated in high vacuum ($\sim 10^{-5}$ torr) and under low apparent contact pressures (0.1–18 kPa) and correlate these changes to the operation lifetime. Sidewall adhesion increased with applied contact pressure. Typically, a twofold to fourfold increase in sidewall adhesion was measured upon cessation of the device operation (typically, $\sim 10^{6}$ sliding cycles) due to the increase of the static friction force above the restoring force available by the device. Scanning electron microscopy (SEM) revealed very small amounts of ultrafine wear debris (10–140 nm) on the sidewall surfaces of about half of the tested devices, without discernible changes in the surface topography. Cross-sectional transmission electron microscopy (TEM) showed that sliding did not cause the removal of the silicon oxide film (5–13 nm in average thickness) from the sidewall surfaces. Atomic force microscopy (AFM) indicated that sliding contact was confined at the top of a few elevated ridges on the sidewall surfaces, resulting in nanoscale wear that smoothened locally the surfaces. SEM, TEM, and AFM results of this study show that the tribological properties of contact-mode MEMS devices operating in high vacuum are controlled by only a few nanoscopic contacts, which depend on the local nanotopography of the interacting surfaces. [2011-0325]**

***Index Terms*—Adhesion, contact pressure, friction, micromachine lifetime, nanoscale wear, nanoscopic contacts, oscillatory sliding, polycrystalline silicon, silicon oxide film, sliding cycles, wear debris.**

Manuscript received November 3, 2011; revised November 27, 2011; accepted December 8, 2011. Date of publication January 27, 2012; date of current version April 4, 2012. This work was supported in part by the Director, Office of Science, Office of Basic Energy Sciences, Division of Materials Sciences and Engineering, of the U.S. Department of Energy under Contract DE-AC02-05CH11231 at the Lawrence Berkeley National Laboratory. Subject Editor H. Seidel.

D. H. Alsem was with the Materials Sciences Division and the National Center for Electron Microscopy, Lawrence Berkeley National Laboratory, Berkeley, CA 94720 USA. He is now with Hummingbird Scientific, Lacey, WA 98516 USA.

H. Xiang and K. Komvopoulos are with the Department of Mechanical Engineering, University of California, Berkeley, CA 94720 USA (e-mail: kyriakos@me.berkeley.edu).

R. O. Ritchie is with the Materials Sciences Division, Lawrence Berkeley National Laboratory, Berkeley, CA 94720 USA, and also with the Department of Materials Science and Engineering and the Department of Mechanical Engineering, University of California, Berkeley, CA 94720 USA.

Color versions of one or more of the figures in this paper are available online at http://ieeexplore.ieee.org.

Digital Object Identifier 10.1109/JMEMS.2011.2180364

I. Introduction

MICROELECTROMECHANICAL SYSTEMS (MEMS) fabricated by low-cost batch processing are used in a wide range of consumer products and defense/space applications, such as chemical, pressure, and acceleration sensors, optical switches, inkjet printer heads, and liquid-crystal display projectors [1]. Many of these microdevices (e.g., micromotors [2], microswitches [3], and digital micromirrors [4]) contain components with load-bearing contact interfaces. As a result of the large surface-to-volume ratio of the microstructures comprising these systems, failure is controlled by micro-/nanoscale surface damage (wear) processes [5], [6]. Because surface interactions assume a dominant role at small length scales, adhesion, electrostatic, and friction forces may exceed inertial forces by several orders of magnitude. Since microstructure, topography, and damage features, such as grains, asperities, and wear debris, respectively, can be of the same order of magnitude as some of the device dimensions (e.g., thickness), changes in the surface topography and formation of fine wear debris may alter significantly the tribological characteristics and, in turn, the device reliability and operation lifetime. Alteration of the adhesion, friction, and electrical characteristics by micro-/nanoscale wear processes could be detrimental to the device functionality and efficiency. Despite significant progress in fabrication processes and design of agile MEMS devices [2], the operation lifetime of such microsystems is still limited by excessive adhesion forces, high wear rates, and rapid evolution of contact fatigue [6], [7]. Cessation of the microdevice operation due to surface degradation and lack of insight into the underlying failure mechanisms are major obstacles, limiting the application range of MEMS.

In contact-mode microdevices, contact stresses should ideally be relatively low to prevent surface damage during operation. In addition, to avoid detrimental environmental effects, devices must be hermetically packaged in vacuum or inert gas atmospheres. However, despite an increasing technological interest on the tribological behavior of MEMS operating under these conditions, there is only a limited amount of data available in the high-vacuum/low-contact-pressure range of operating parameters of contact-mode microdevices. Although multiasperity contact phenomena in micromachined polycrystalline silicon (polysilicon) have been investigated extensively using on-chip device testing under controlled contact load and environmental conditions [8]–[26], tribological studies for high-vacuum/low-contact-pressure conditions are sparse. It has been

reported that wear of polysilicon in vacuum commences with the removal of the native oxide layer, followed by asperity fracture or grain pull-out of the exposed silicon surface [27]. Longer lifetime of lateral motors has been reported for operation in air than in vacuum for contact loads in the micronewton–newton range [28], [29]. The static friction coefficient of polysilicon contact-mode microdevices operated in vacuum under loads in the micronewton range has been reported to increase nonlinearly with the apparent contact pressure [30]. Surface micromachines suitable for studying sidewall adhesion under much lighter loads (in the nanonewton range), resulting in mean contact pressures on the order of kilopascals, were used to study the contribution of contacting and noncontacting asperities to the total adhesion force [31], [32] and measure the true static coefficient, which includes contributions from both van der Waals and capillary forces to the applied normal load [33]. Insight into the wear behavior of sidewall surfaces has been obtained from transmission electron microscopy (TEM) studies of collected wear debris and by monitoring the evolution of the static adhesion force in the course of oscillatory sliding contact of devices operated in high vacuum under relatively high contact pressures [34].

A review of the literature suggests that basic understanding of multiasperity contact interactions in contact-mode MEMS devices operated in high vacuum and under low contact pressures is limited. Therefore, the objective of this study was to investigate the high-vacuum tribological behavior of polysilicon sidewall surfaces subjected to apparent contact pressures of a few kilopascals. The adhesive contact pressure was used as an *in situ* indicator of the evolution of the surface morphology during reciprocating sliding of the sidewall surfaces. Changes in the surface morphology after a given number of sliding cycles and insight into the governing wear process were obtained from scanning electron microscopy (SEM), TEM, and atomic force microscopy (AFM) studies. Results and interpretations presented hereinafter are directly applicable to the design and fabrication of reliable polysilicon devices possessing contact interfaces.

II. Experimental Procedures

A. Fabrication and Description of Testing Microdevice

On-chip n^+-type polysilicon MEMS devices, specifically designed for sidewall friction and wear testing [31]–[33], were fabricated by the PolyMUMPs fabrication process [35]. Polysilicon layer deposition and etching were accomplished by low-pressure chemical vapor deposition and reactive ion etching, respectively. After the removal of the photoresist by two 25-min acetone baths, the devices were released by rinsing with isopropanol and drying in air. The die was then submerged into a bath of 49% buffered hydrofluoric acid for 2.5 min and, subsequently, rinsed with deionized water for 10 min and isopropyl alcohol also for 10 min. To eliminate device stiction due to liquid meniscus formation, the final step of the release process comprised carbon dioxide supercritical point drying.

The test device consists of two suspended shuttles, referred to as the loading and sliding shuttles, driven laterally by electrostatic comb drives [Fig. 1(a)]. First, normal contact between the sidewall surfaces was established by applying a dc bias voltage to the comb drive of the loading shuttle in order to push it against a protrusion of width equal to 5, 10, or 20 μm extending from the sidewall surface of the sliding shuttle [Fig. 1(b)]. Then, oscillatory sliding contact was initiated by applying sinusoidal ac signals to the comb drive of the sliding shuttle, causing the protrusion to slide against the sidewall surface of the loading shuttle. Relationships of the forces acting during sliding contact [Fig. 1(b)] and the true and engineering friction coefficients can be found in previous publications [15], [31]–[34].

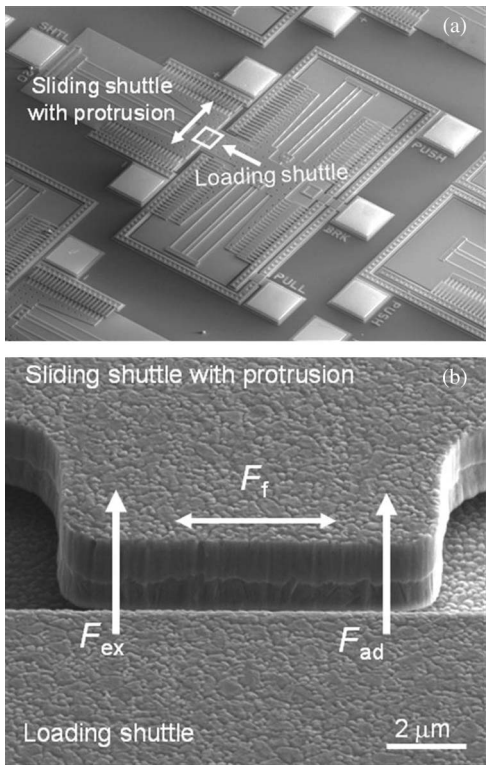

Fig. 1. SEM micrographs of (a) entire test device showing the loading and sliding shuttles and (b) contact region [enclosed within a square frame in (a)] showing a protrusion on the sliding shuttle facing the sidewall surface of the loading shuttle. The viewing angle in (b) is 52° from the normal to the top surface of the sliding shuttle. ($F_{\rm ex}$ is external force, $F_{\rm ad}$ is adhesion force, and F_f is friction force.)

B. Experimental Apparatus

Adhesion and sliding tests were carried out with a multiprobe vacuum station (MMR Technologies) mounted on a vibration isolation table (Newport Electronics). Voltages were applied to the comb drives and the shuttles through tungsten probe tips connected to dc power sources (Agilent E3612A). The oscillatory movement of the sliding shuttle was monitored with a stereomicroscope (Olympus SZ-CTV series). Digital images were obtained with a charge-coupled-device camera (Sony DXC-390P). With the present optical system, device displacements as small as ~ 0.3 μm could be detected, which was sufficient for the tests of this study. All tests were performed under a chamber pressure of $\sim 10^{-5}$ torr, a temperature between 20 °C and 30 °C, an oscillation frequency fixed at 25 Hz, and a

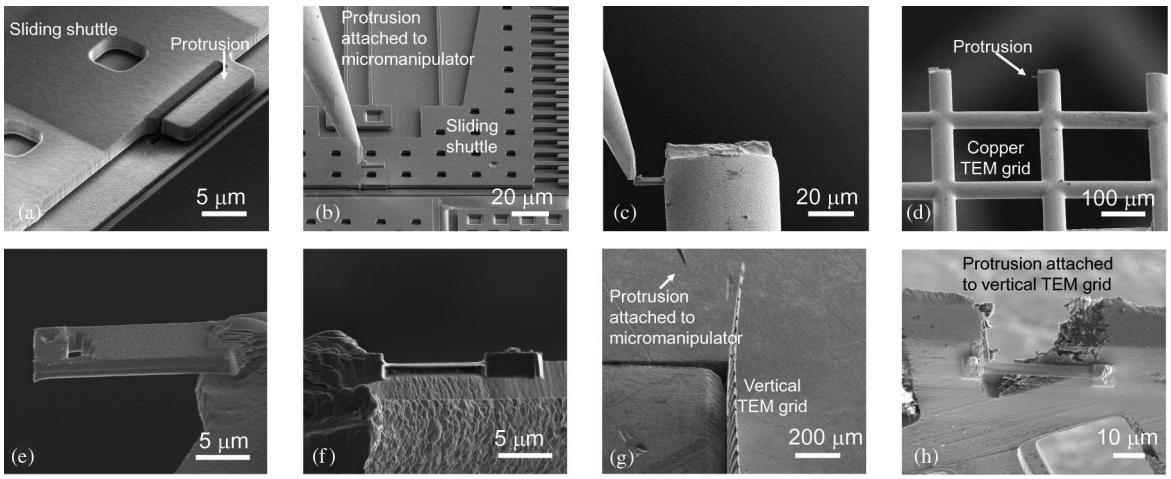

Fig. 2. Representative SEM micrographs of the sample preparation process. TEM samples were obtained by (a) FIB cutting of the protrusion from the sliding shuttle, (b) attaching the protrusion to a tungsten micromanipulator, (c and d) transferring the protrusion to a horizontal TEM copper grid, and (e and f) thinning the sample with the protrusion to electron transparency ($\sim$100 nm). AFM samples were obtained by (g) transferring the protrusion attached to the tungsten micromanipulator to a vertical TEM copper grid and (h) orienting the sample in the horizontal direction, such that the protrusion sidewall surface faces the upward direction.

normal load varied in the range of 11–145 nN, with a corresponding mean (apparent) contact pressure range of 0.1–18 kPa. Typical peak-to-peak sliding amplitudes were in the range of 3–8 μm. Since a sliding cycle is equal to two times the peak-to-peak amplitude, the sliding speed was varied between 150 and 400 μm/s. Additional details about the operation of the test device used in this investigation can be found elsewhere [31]–[34].

C. Microanalysis Techniques

Changes in the surface morphology and formation of wear debris on the sliding sidewall surfaces were observed with a scanning electron microscope (Zeiss Supra 55VP) and a dual-beam focused-ion-beam (FIB) system (FEI Strata DB235) operated at 5 kV. More detailed information of the sidewall surface topographies was obtained with an atomic force microscope (Veeco Digital Instruments Nanoscope IIIa) operated in noncontact mode, using single-crystal Si tips of nominal radius of curvature equal to 5 nm (Nanoworld Pointprobe). Horizontal cross sections of the near-surface microstructure of sidewall surfaces were examined by analytical TEM and energy-filtered TEM using a 300-kV JEOL 3010 (with LaB_6 filament) and a 200-kV Philips CM200FEG (field emission gun) equipped with a Gatan image filter, respectively. AFM and TEM samples were prepared with the previously mentioned dual-beam FIB using a tungsten micromanipulator (Omniprobe) (Fig. 2). Worn protrusions were cut from the sliding shuttles with the FIB [Fig. 2(a)] and moved to a TEM copper grid using the tungsten micromanipulator [Fig. 2(b)] onto which they were temporarily welded with Pt [Fig. 2(c)–(e)]. FIB thinning of these protrusions [Fig. 2(e) and (f)] to electron transparency ($\sim$100 nm) was performed after the deposition of protective Pt layers onto the surface exposed to the ion beam. First, a Pt layer was deposited by electron-beam evaporation to protect the sample from damage during ion-beam deposition of a second thicker layer. To thin down the sample, slices perpendicular to the sliding surface were milled off, starting from the side of the sample protected by the Pt layer, i.e., opposite to the side that had been in sliding contact [Fig. 2(f)]. This was necessary to prevent ion implantation during thinning and subsequent damage of the sliding surface. The drawback of thinning from the opposite side is that some material may be redeposited on the side of interest. For the final thickness of the TEM sample, the sampling percentage of the total apparent area of contact was 5%, which is significantly larger than the typical real-to-apparent contact area ratio, implying that any global wear within the surface layer should be visible in the TEM sample.

AFM samples were prepared by FIB sample preparation techniques similar to that of the TEM samples [Fig. 2(a) and (b)]. However, in contrast to the TEM samples for which the grids were placed horizontally, the TEM copper grid of the AFM samples was positioned vertically before the sample attachment [Fig. 2(g) and (h)]. The grid was then placed horizontally to orient the sidewall surface in the upward direction for subsequent AFM imaging. Surface height data obtained with the AFM were used to calculate the root-mean-square (rms) roughness and the power spectral density (PSD) function of sidewall surfaces scanned before and after testing. AFM images (512×512 pixels) of 2×2 μm^2 surface areas were analyzed by 512 line scans obtained along the sliding direction. To evaluate topographical differences in the sliding direction, PSD functions of the slid surfaces were then obtained as averages of the PSD functions determined from the aforementioned line scans. To further examine nanotopography differences between the sliding and the original surfaces, standard deviations of corresponding PSD functions were contrasted in the low-wavelength range.

III. Results

A. Adhesion and Dynamic Friction

Fig. 3 shows the variation of the mean adhesive pressure (defined as the measured adhesive force divided by the

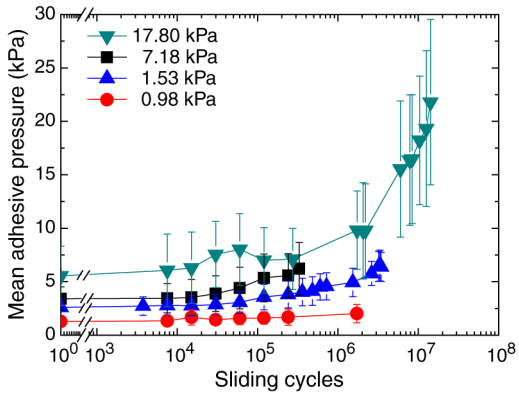

Fig. 3. Mean adhesive pressure versus sliding cycles for mean contact pressure in the range of 0.98–17.8 kPa. Data points represent mean values of 25 measurements, i.e., five measurements per location × five different locations on the protrusion sidewall surface of the sliding shuttle. Error bars indicate one standard deviation above and below the corresponding mean value.

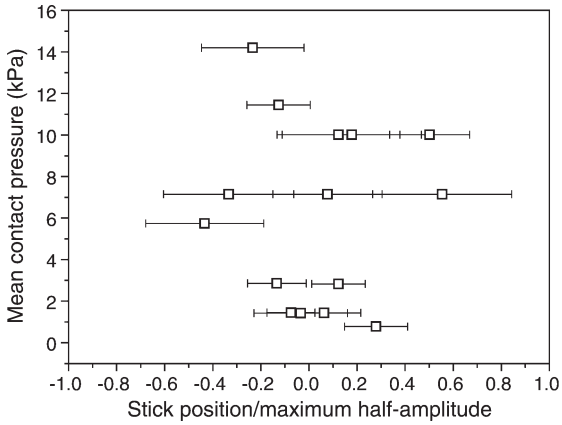

Fig. 4. Mean contact pressure versus position of cessation of the device movement due to stiction normalized by the maximum distance (half amplitude) measured initially during oscillatory sliding contact. Data points represent mean values of five measurements obtained with one device at a given mean contact pressure. Error bars indicate one standard deviation above and below the corresponding mean value.

apparent contact area between the protrusion of the sliding shuttle and the sidewall surface of the loading shuttle) with sliding cycles for mean contact pressure in the range of 0.98–17.8 kPa. The statistical results shown in this figure were obtained from four devices. Each point represents the mean value of 25 measurements, i.e., five adhesion measurements obtained from five different locations of the sliding track of each device operated for a given number of sliding cycles. Thus, error bars represent local experimental scatter as well as location-to-location scatter along the sliding track. The general trend is for sidewall adhesion to increase with both sliding cycles and mean contact pressure. For all contact pressures, a fairly stable adhesive behavior was observed up to $\sim 10^5$ sliding cycles (incubation period), followed by an increase in adhesive pressure by a factor of two to four (depending on the mean contact pressure) in the range of 10^5–10^6 sliding cycles, with the eventual cessation of the oscillatory movement (stiction) of the device sliding under the highest contact pressure (17.8 kPa).

Fig. 4 shows the dimensionless stick position of 15 devices for a mean contact pressure in the range of 0.98–17.8 kPa.

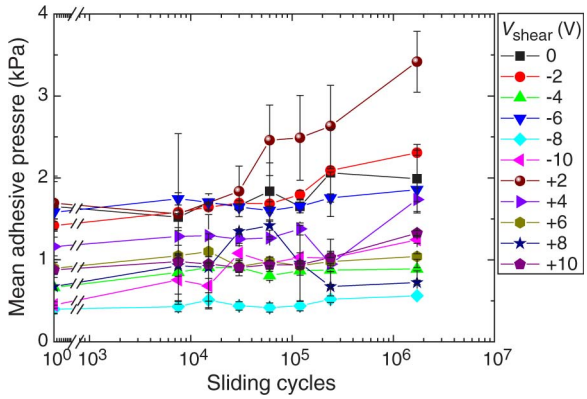

Fig. 5. Mean adhesive pressure versus sliding cycles for different positions along the sliding track, obtained by applying different voltages V_{shear} (from -10 to $+10$ V) to the comb drive of the sliding shuttle.

The dimensionless stick position is defined as the ratio of the position of the sliding shuttle at the instant that oscillatory movement ceased to the oscillation amplitude at the onset of sliding under a given mean contact pressure. Two interesting trends can be identified: 1) 11 (77%) of the devices ceased sliding within the center region of the oscillation amplitude (i.e., within $\pm 30\%$ of the dynamic amplitude measured from the rest position), and 2) variation of the mean contact pressure by more than an order of magnitude did not change the general trend of device stiction to occur within the center region of the sliding track. Plotting these data in the form of a histogram yielded a fairly symmetric distribution of devices that ceased sliding due to stiction at about the zero-amplitude point, confirming the general trend revealed by the results shown in Fig. 4.

The relation between adhesion and stick position was further examined by measuring the mean adhesive pressure at different distances from the zero-displacement point as a function of sliding cycles. This involved interrupting each test after a given number of sliding cycles, displacing the sliding shuttle from the zero-amplitude position to the desired position by applying a dc bias voltage (referred to as V_{shear}) to the comb drive of the sliding shuttle, and measuring the adhesive pressure as described previously. Representative results from these experiments are shown in Fig. 5. Generally higher adhesion and/or faster increase in adhesion were found within the center region of the sliding track (-2 V $\leq V_{\mathrm{shear}} \leq 2$ V), revealing a correlation between the increase in adhesive pressure and failure (stick) position.

Among the 32 devices tested, three devices ($\sim$9%) did not stick even after 10^7 sliding cycles (at which instant sliding was terminated), four devices ($\sim$13%) failed before reaching 10^5 sliding cycles, and 25 devices ($\sim$78%) ceased movement after 10^5–10^7 sliding cycles. For the latter devices, the average number of sliding cycles to stiction was equal to $\sim 2 \times 10^6$, regardless of the mean contact pressure. The sliding cycles to stiction of devices operated in the mean contact pressure ranges of 1–2, 2–4, 4–10, and 10–18 kPa varied by a factor of approximately ten, indicating significant device-to-device variation.

The engineering and true friction coefficients for mean adhesive pressure between 7.15 and 12.87 kPa measured before sliding and after stiction are given in Table I. The data represent

TABLE I
ENGINEERING AND TRUE FRICTION COEFFICIENTS μ_e AND μ_t, RESPECTIVELY, MEASURED BEFORE SLIDING AND AFTER DEVICE FAILURE (STICTION) VERSUS MEAN ADHESIVE PRESSURE p_{ad}

Mean adhesive pressure (p_{ad}) (kPa)	Engineering friction coefficient (μ_e)		True friction coefficient (μ_t)	
	before sliding	after stiction	before sliding	after stiction
7.15	1.41	0.65	1.06	0.38
10.01	0.63	1.02	0.31	0.11
11.44	0.63	0.71	0.54	0.29
12.87	0.60	0.63	0.67	0.47
12.87	0.58	0.32	0.55	0.16

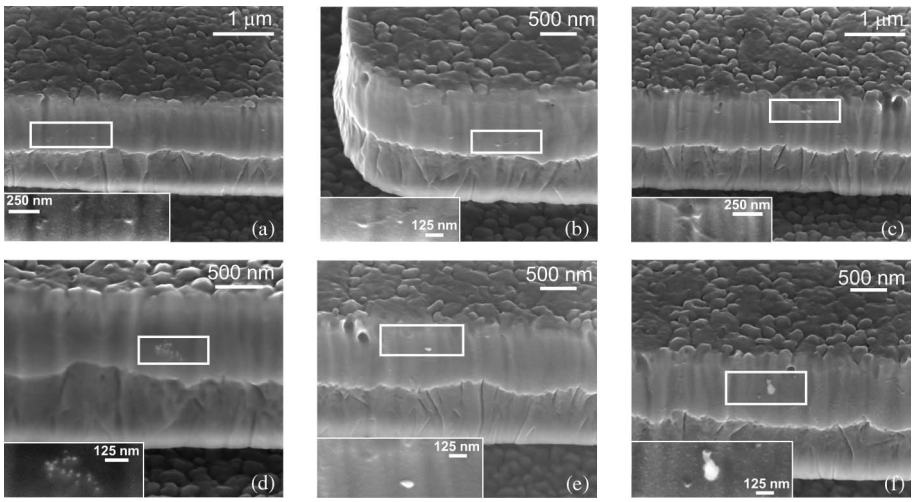

Fig. 6. SEM micrographs of sidewall surfaces showing (a and b) surface contaminants before sliding and (c–f) formation of fine wear debris due to sliding. Contamination particles and wear debris are distinguished by rectangular frames and shown at high magnifications in the insets of figures. Sliding surfaces contain both (a) surface contamination particles and (d–f) ultrafine (10–140 nm) wear debris (bright contrasting particles).

averages of five measurements obtained with the same device for a given mean adhesive pressure. Changes in the engineering friction coefficient from the onset of sliding up to the instant of stiction do not show a consistent trend. This is attributed to the significant contribution of the adhesion force to the total normal force at relatively low and moderate contact pressures [33], which is not included in the calculation of the engineering friction coefficient. Conversely, the true friction coefficient, which includes the effect of the adhesive force [33], measured after stiction is consistently lower than that measured before sliding. Although the change in the true friction coefficient indicates that sliding induced surface changes, the directly measurable parameter that dominates the true coefficient of friction is the adhesive force. Therefore, the mean adhesive pressure is a suitable parameter for tracking surface changes during oscillatory sliding contact.

B. Sidewall Surface Morphology

SEM images of sidewall surfaces obtained before sliding revealed the presence of small amounts of surface contaminants [Fig. 6(a) and (b)]. Clearly contrasting wear debris was found on some of the sliding sidewall surfaces [Fig. 6(d)–(f)], in addition to surface contaminant particles that had survived surface rubbing [see the inset in Fig. 6(c)]. This suggests that a wear-debris-generating mechanism was active during sliding. However, as observed by SEM, sliding did not produce any other discernible surface changes, such as pits or microcracks. The surface dimples shown in Fig. 6(e) and (f) were also observed on the as-fabricated sidewall surfaces. Wear debris was usually only present in one or two locations and mostly in very small quantities [see the insets in Fig. 6(d)–(f)]. Wear debris observations made with devices tested under various contact loads (pressures) and for different durations are summarized in Table II. Among the 26 devices inspected, 11 (42%) contained wear debris, with larger debris (50–140 nm) appearing to be agglomerates of smaller (10–50 nm) wear particles, which were not possible to be determined from the SEM images if they were also agglomerates of even smaller particles.

In addition to these types of wear debris, another type of surface particles was found not only after but also before sliding [see the insets in Fig. 6(a) and (b)]. These particles were likely organic contaminants generated by the release process, which also includes the removal of a photoresist layer [35]. Energy

TABLE II
AVERAGE SIZE OF WEAR DEBRIS d DETECTED ON SIDEWALL SURFACES OF TESTED DEVICES VERSUS EXTERNAL NORMAL FORCE F_{ex}, MEAN CONTACT PRESSURE p_{ex}, AND SLIDING CYCLES N

Device number	F_{ex} (nN)	p_{ex} (kPa)	N ($\times 10^4$)	d (nm)	Device number	F_{ex} (nN)	p_{ex} (kPa)	N ($\times 10^4$)	d (nm)
SI-1	75	9.4	180	Ø	HV-5	57.6	1.5	100	~50
SI-2	75	2.0	180	20–30	HVI-1	57.1	1.5	231	10–95
SI-3	75	4.2	180	Ø	HVI-4	57.8	1.5	94	25–140
HI-1	71.0	8.9	449	Ø	HVII-1	100.1	12.5	55.7	Ø
HI-2	84.1	10.5	547	Ø	HVII-2	114.4	14.3	22.4	Ø
HI-3	96.5	12.1	292	Ø	HVII-3	128.7	16.1	0.0225	Ø
HI-4	11.6	0.12	1560	20–30	HVII-4	71.5	8.9	123	10–50
HIII-1	57.2	1.5	734	60–120	HVII-5	128.7	16.1	1260	Ø
HIII-2	90.4	5.0	353	~40	HVII-6	100.1	12.5	205	Ø
HIII-3	50.1	2.8	36.2	Ø	HVII-7	100.1	12.5	168	Ø
HIII-4	57.2	3.2	28.5	45–135	HVIII-1	57.2	3.2	4.2	Ø
HV-1	56.6	3.1	8.9	10–90	HVIII-2	143	7.9	578	Ø
HV-4	57.8	1.5	94	25–75	HVIII-4	142	17.8	1335	Ø

Ø = no observable wear debris

dispersive X-ray spectroscopy (EDS) analysis of a large (several micrometers) cluster of this residue remotely from the sliding track and a clean area of the structural layer (reference spectrum) showed the presence of carbon and oxygen peaks only in the EDS spectrum of the contaminant cluster, indicating that it was most likely organic in nature. Although SEM imaging often results in carbon deposition onto the imaged surface, the distinct differences in the EDS spectra of the contaminant cluster and the reference surface in conjunction with the presence of oxygen are clear evidence of an organic contaminant residue.

The SEM micrographs shown in Fig. 6 contain a horizontal etch line about halfway in all sidewall surfaces. The effect of this feature on the sidewall contact profile was analyzed using FIB cross sections. It was found that, although contact did not occur along the etch line over a region of ~170 nm in height, (apparent) contact occurred over most of the rest of the 2-μm height of the sidewall surfaces. In the mean contact pressure calculations, an upper-bound apparent contact area that includes the full sidewall height was assumed. In addition, the tapering angle of the sidewall surfaces was found to be very small ($\sim 2^\circ$).

C. Sidewall Surface Microstructure

Further insight into the formation of wear debris was obtained from horizontal TEM cross-sectional images of the sidewall surfaces. Fig. 7 shows typical bright-field and energy-filtered TEM images of oxygen distribution in horizontal cross sections of protrusions obtained before and after sliding. Table III shows a comparison between the global silicon oxide film thickness along the full length of the protrusions of three devices measured after sliding and that measured over a similar reference section outside the sliding track of the same device. In both cases, the sampling size represents 5% of the total apparent area of contact. These measurements show an average silicon oxide thickness of ~9 nm before sliding and a similar thickness after sliding. In addition, the data given in Table III indicate that the silicon oxide film thickness was not affected by the external force (mean contact pressure) during sliding. These measurements indicate that the silicon oxide film thickness did not undergo discernible global changes even after $(2-7) \times 10^6$ sliding cycles, despite the fact that wear debris was observed after sliding (Fig. 6).

D. Sidewall Surface Roughness and Spectral Power Density Function

In addition to electron microscopy, the evolution of the sidewall surface topography due to surface rubbing was studied with the AFM. The topography of the sidewall surface slid against the protrusion of a micromachine that did not show formation of wear debris was examined [Fig. 8(a)], and the rms roughness values inside and outside the sliding track (obtained

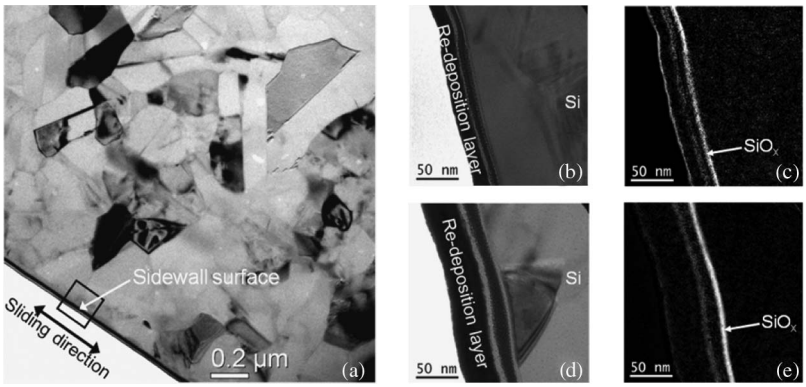

Fig. 7. Cross-sectional TEM images of original and sliding sidewall surfaces: (a) image of sidewall surface showing the polysilicon grains, cross sections of (b) original and (d) sliding sidewall surfaces, and (c and e) energy-filtered images showing the distribution of oxygen in the (c) original and (e) sliding sidewall surfaces shown in (b) and (d), respectively.

TABLE III
SILICON OXIDE FILM THICKNESS (MEASURED BEFORE AND AFTER SLIDING) VERSUS EXTERNAL NORMAL FORCE F_{ex}, MEAN CONTACT PRESSURE p_{ex}, AND SLIDING CYCLES N

Device number	F_{ex} (nN)	p_{ex} (kPa)	N ($\times 10^6$)	Silicon-oxide film thickness (nm)	
				before sliding	after sliding
HI-3	96.5	12.1	2.92	10 ± 2	11 ± 3
HIII-1	57.2	1.5	7.34	7 ± 2	7 ± 2
HIII-2	90.4	5.0	3.53	11 ± 4	10 ± 3

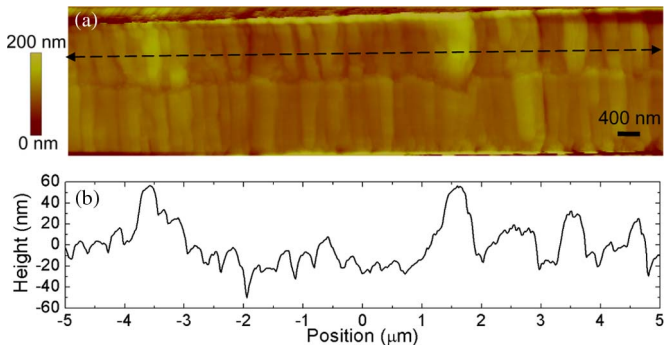

Fig. 8. (a) AFM image of the sidewall surface of a loading shuttle obtained after 1.3×10^7 sliding cycles and (b) surface profile corresponding to the dashed line shown in (a) revealing the presence of only a few raised ridges that controlled the real area of contact during sliding.

as the average of seven and nine roughness values, respectively, calculated from 2×2 μm^2 AFM scan areas) were found equal to 11 ± 3 and 12 ± 2 nm, respectively. Two-dimensional profile traces [Fig. 8(b)] revealed that only a few raised ridges of the sidewall surfaces participated in sliding, indicating that the real area of contact was several orders of magnitude smaller than the apparent area of contact. This implies that any possible surface alterations were confined at the tops of few raised ridges.

Despite the fact that surface sliding was confined at the highest ridges of the sidewall surfaces, AFM examination of the nanotopographies of ridges inside and outside the sliding track did not reveal any discernible differences. However, PSD plots obtained from 2×2 μm^2 AFM scans revealed fine topographical differences between the sliding track and the original surface. The PSD intensity at the center region of the sliding track demonstrated a decreasing trend in the low-wavelength range [Fig. 9(a)] compared to that of the original surface [Fig. 9(b)]. The decrease in PSD intensity in the low-wavelength range suggests that topography changes due to surface sliding were nanoscopic. This implies that localized smoothening of the sliding track nanotopography was induced by a nanoscale wear process. To further illustrate that sliding indeed altered the nanotopography, standard deviations of the PSD functions shown in Fig. 9(a) and (b) plotted in the low-wavelength range $(10^{-1}-10^{-2}$ μm) are contrasted in Fig. 9(c). The higher standard deviation of the PSD function of the sliding track than that of the original surface indicates a consistently higher variability in surface feature sizes in the low-wavelength range of the sliding track topography. This is further evidence that a nanoscale wear process (not detectable even at high magnifications) was responsible for the observed nanoscopic surface changes that resulted in the increase of the adhesion force and ultimate cessation of the device movement.

IV. DISCUSSION

The results presented in the previous section indicate that localized changes in the nanotopography of the sliding surfaces may exhibit a profound effect on the adhesion characteristics of contact-mode MEMS devices operated in high vacuum. Nanoscale surface changes were tracked by observing the evolution of the apparent adhesion force (mean adhesive

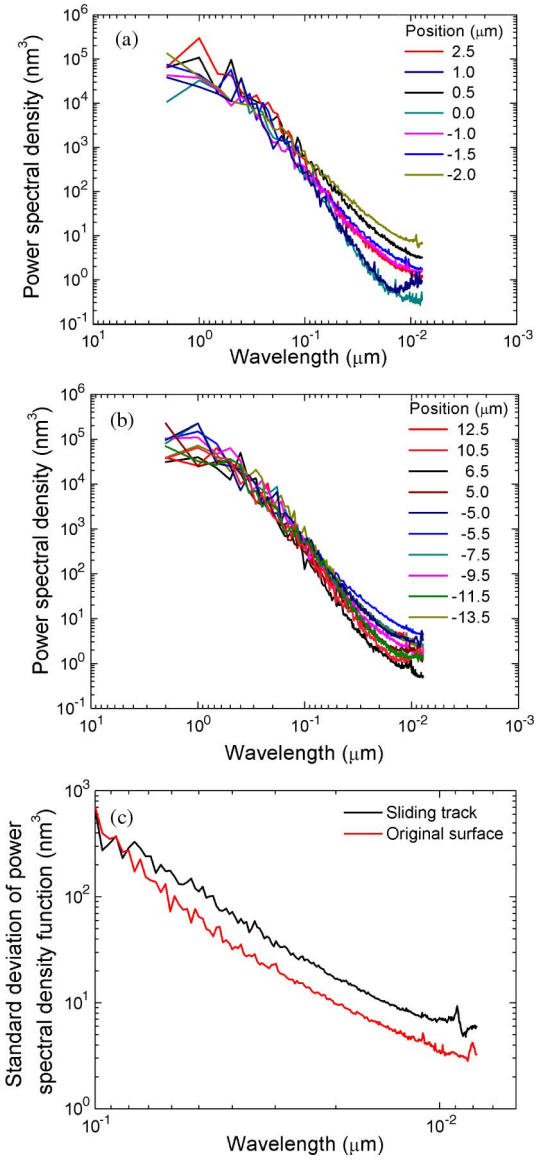

Fig. 9. Power spectral densities of (a) sliding and (b) original sidewall surfaces obtained from $2 \times 2\ \mu m^2$ AFM scans of different surface locations and (c) standard deviations of the power spectral densities of the sliding and original sidewall surfaces with spectra shown in (a) and (b), respectively, versus wavelength.

pressure) with the number of sliding cycles. The observed friction and wear behaviors of the sliding sidewall surfaces can be interpreted in the context of a mechanistic process, based on the measured adhesion force and SEM, TEM, and AFM observations.

A. Adhesion and Device Failure

The increase in adhesion (Fig. 3) correlated with the increase in sidewall surface friction (Table I), indicating that surface modification occurred during sliding despite the low contact pressure, ultimately causing the device to cease movement. The adhesion increase with contact pressure (Fig. 3) is attributed to the increase of the real area of contact and is consistent with similar observations of an earlier study [30]. The increase of the mean contact pressure resulted in a more pronounced increase in adhesive pressure (Fig. 3). This can be associated with more extensive surface modification due to the intensification of surface interaction with the increase of the contact pressure. This trend is similar to that encountered in traditional tribology, i.e., the wear volume increases with the applied normal load, known as Archard's wear law [36], [37].

For most of the tested devices, operation ceased around the neutral position of the sliding shuttle (i.e., approximately zero amplitude), independent of the contact pressure applied during sliding (Fig. 4). Moreover, the average number of sliding cycles for the device movement to cease (stiction) did not correlate with the mean contact pressure, suggesting a similar failure mechanism in all the experiments and that the highest adhesion (or adhesion increase) predominantly occurred within a relatively small distance from the neutral position. This was confirmed by observing the evolution of the adhesive pressure at various positions along the sliding track (Fig. 5). The tendency for stiction to occur around the zero-amplitude position can be explained by considering the forces acting on the sliding shuttle at zero- and maximum-amplitude positions. At zero-amplitude position, the restoring force is zero and the tangential force (opposed by the friction force) is the maximum electrostatic force generated by the comb drives of the sliding shuttle. However, maximum restoring and electrostatic forces of equal magnitude are produced at maximum-amplitude position. Because the resulting tangential force in this case is about two times higher than that at zero-amplitude position, it is more likely for device stiction to occur within the center region of the sliding track, as evidenced from the data shown in Fig. 4.

B. Surface Morphology and Wear Mechanisms

Despite the evidence that nanoscale surface changes were responsible for the cessation of the device operation (Figs. 3–5), it was not possible to identify directly the surface morphology that governed device failure due to stiction. Although wear debris was found on the sidewalls of 42% of the tested devices (Fig. 6 and Table II), wear particles were not observed with all devices, or they were of extremely small quantities. In addition, changes in surface roughness due to sliding were statistically insignificant, and the thickness of the silicon oxide surface layer did not show a clear trend to decrease even after $(2-7) \times 10^6$ sliding cycles (Fig. 7 and Table III). However, these results cannot accurately reveal nanoscale topography changes in a few random locations. For example, local wear of the oxide layer could have been obscured by the inherent variation of its thickness (Table III). The presence of wear debris in 42% of the tested devices observed with the SEM (Fig. 6 and Table II) and the fact that any discernible changes in surface morphology were not detected by the TEM (Fig. 7 and Table III) are evidence of a random local wear process operating at the nanoscale. This conclusion is also supported by the decrease of the sliding track's PSD intensity in the low-wavelength range [Fig. 9(a)] and its larger variation along the sliding direction [Fig. 9(c)], indicating that localized surface smoothening occurred by a nanoscale wear process. Furthermore, because both AFM and TEM sample preparations are destructive processes (Fig. 2), these methods do not allow for

direct comparison of exactly the same sidewall area before and after sliding. Therefore, it is extremely difficult to accurately capture changes in nanoscale surface morphology due to a random nanoscale wear process.

An important deduction from the lack of significant average wear of the silicon oxide layer (Fig. 7 and Table III) is that wear occurred within the silicon oxide layer and not in the polysilicon. Because of galvanic oxidation of devices containing gold-coated features during the HF release step of the PolyMUMPs process [38]–[40], these oxide layers are thicker [$\sim$9 nm, as shown in Fig. 7(c) and (e)] than typical native oxide layers of polysilicon surfaces (typically, $\sim$3 nm thick [39]). Thus, if the oxide layer was worn off during sliding, it would have regenerated as an $\sim$3-nm-thick native oxide layer. However, this is not the case, as evidenced in Fig. 7 and Table III. Because an oxide layer thicker than the native oxide layer and wear debris were found on the sidewall surfaces after sliding, it is concluded that wear was confined at the surface of the thermal silicon oxide layer. The absence of wear-induced surface pits and scars on the sidewall surfaces [Figs. 6 and 8(a)] indicates that local nanoscale wear of the silicon oxide layer was the governing process of material removal under the present sliding conditions. In about half of the tested devices, small wear particles [Fig. 6(d)] were observed to cluster, forming larger agglomerates [Fig. 6(f)]. From a MEMS design point of view, this implies that, for contacting polysilicon surfaces under low contact pressure, the tribological behavior of the silicon oxide layer is of critical importance, even after a large number of sliding cycles. In addition to nanoscale wear of the silicon oxide layer, the removal and/or smoothening (smearing) of the organic contaminant detected on the sidewall surfaces [Fig. 6(a)–(c)] is potentially another mechanism that could have contributed to the increase in sidewall adhesion, leading eventually to device failure due to stiction. Both of these morphological effects are highly localized and differ from device to device, yet they control the tribological behavior of the sidewall surfaces. This argument is supported by the following: 1) the lack of measurable changes in the average surface morphology, despite the fact that wear debris was found on almost half of the tested devices; 2) the occurrence of sliding contact at only few small surface regions at the top of raised ridges on the sidewall surfaces [Fig. 8(b)]; 3) the spatial variation of adhesion within the sliding track (Fig. 5); and 4) the relatively large scatter in the operation life of the tested devices (10^5–10^6 sliding cycles).

Comparing the results of this study with those of previous studies obtained in vacuum but under higher contact loads (pressures) [27], [28], [34], the devices of the present study show virtually no wear debris and no discernible changes in surface morphology. Despite the lack of clear surface degradation [Figs. 6, 7, and 8(a)], it is apparent that surface modification occurred during the several million sliding cycles (Fig. 9), leading to cessation of the device movement (Figs. 3–5). These findings suggest that alteration of the sidewall surface morphology and, presumably, physicochemical properties, even under very mild contact conditions, may be the governing factor in the lifetime of contact-mode MEMS devices. The results of this study show that these technologically important low-contact-pressure conditions may lead to extremely small (nanoscopic) changes in surface morphology, which can only be detected by very detailed characterization, making large-scale routine morphological inspection of these surfaces a nontrivial challenge.

V. Conclusion

Changes in the adhesion and morphology of sidewall surfaces of polysilicon MEMS devices operated in high vacuum ($\sim 10^{-5}$ torr) and under relatively low apparent contact pressure ($\sim$1–18 kPa) were examined in the context of mean adhesive pressure, coefficient of friction, and device lifetime measurements as well as microanalysis results. Despite the low apparent contact pressures, sidewall adhesion increased during oscillatory sliding, eventually leading to cessation of the device movement (stiction), mainly within the center region of the sliding track. The adhesion force after the instant of stiction (typically, after $\sim 10^6$ sliding cycles) was found to be higher than that of the original surface by a factor of two to four.

Very small amounts of fine debris (10–140 nm in average size) were observed on the sidewalls of about half of the tested devices without any discernible changes in surface morphology. In addition, organic contaminants from the release process were detected before and after sliding. The average thickness of the silicon oxide surface layer ($\sim$9 nm), measured by cross-sectional TEM, did not show any decrease as a result of sliding, indicating that a localized nanoscale wear process was active at the surface of the silicon oxide layer.

AFM studies of the sidewall morphology revealed that only a few raised ridges were in contact during sliding. Power spectrum density analysis showed that sliding induced nanoscale surface smoothening of those ridges. These findings indicate that a random nanoscale wear process, confined at the surface of the thermal silicon oxide layer, was responsible for the observed localized smoothening of the surface nanotopography. Despite the lack of any detectable wear features on the sliding surfaces, this nanoscale wear process increased the interfacial adhesion, leading eventually to device stiction. These nanoscale changes in surface morphology indicate that adhesion and wear were determined by only a few nanoscopic contacts that were strongly dependent on the local topography. This explains the significant scatter in the number of sliding cycles leading to device failure (stiction) and suggests that, even under very low contact pressures and high-vacuum conditions, the lifetime of contact-mode polysilicon MEMS devices may be limited by surface adhesion effects.

Acknowledgment

Electron microscopy was carried out at the National Center for Electron Microscopy operated at the Lawrence Berkeley National Laboratory with the support of the U.S. Department of Energy under Contract DE-AC02-05CH11231.

References

[1] N. Maluf and K. Williams, *An Introduction to Microelectromechanical Systems Engineering*. Boston, MA: Artech House, 2004.

[2] W.-M. Zhang and G. Meng, "Friction and wear study of the hemispherical rotor bushing in a variable capacitance micromotor," *Microsyst. Technol.*, vol. 12, no. 4, pp. 283–292, Mar. 2006.

[3] J. Lampen, S. Majumder, R. Morrison, A. Chaudhry, and J. Maciel, "A wafer-capped, high-lifetime ohmic MEMS RF switch," *Int. J. RF Microw. Comput. Aided Eng.*, vol. 14, no. 4, pp. 338–344, Jul. 2004.
[4] A. Jain and H. Xie, "A single-crystal silicon micromirror for large bi-directional 2D scanning applications," *Sens. Actuators A, Phys.*, vol. 130/131, pp. 454–460, Aug. 2006.
[5] K. Komvopoulos, "Surface engineering and microtribology for microelectromechanical systems," *Wear*, vol. 200, no. 1/2, pp. 305–327, Dec. 1996.
[6] A. D. Romig, Jr., M. T. Dugger, and P. J. McWhorter, "Materials issues in microelectromechanical devices: Science, engineering, manufacturability and reliability," *Acta Mater.*, vol. 51, no. 19, pp. 5837–5866, Nov. 2003.
[7] D. H. Alsem, O. N. Pierron, E. A. Stach, C. L. Muhlstein, and R. O. Ritchie, "Mechanisms for fatigue of micron-scale silicon structural films," *Adv. Eng. Mater.*, vol. 9, no. 1/2, pp. 15–30, Feb. 2007.
[8] M. G. Lim, J. C. Chang, D. P. Schultz, R. T. Howe, and R. M. White, "Polysilicon microstructures to characterize static friction," in *Proc. IEEE Electro Mech. Syst.*, 1990, pp. 82–88.
[9] M. Mehregany, S. D. Senturia, and J. H. Lang, "Friction and wear in microfabricated harmonic side-drive motors," in *Tech. Dig., Solid-State Sens. Actuator Workshop*, Hilton Head Island, SC, 1990, pp. 17–22.
[10] M. Mehregany, S. D. Senturia, and J. H. Lang, "Measurement of wear in polysilicon micromotors," *IEEE Trans. Electron Devices*, vol. 39, no. 5, pp. 1136–1143, May 1992.
[11] S. T. Patton, W. D. Cowan, and J. S. Zabinski, "Performance and reliability of a new MEMS electrostatic lateral output motor," in *Proc. 37th Annu. Int. Rel. Phys. Symp.*, San Diego, CA, 1999, pp. 179–188.
[12] M. P. de Boer, J. M. Redmond, and T. A. Michalske, "A hinged-pad test structure for sliding friction measurement in micromachining," in *Proc. SPIE—Int. Soc. Opt. Eng.*, 1998, vol. 3512, pp. 241–250.
[13] E. E. Flater, A. D. Corwin, M. P. de Boer, and R. W. Carpick, "*In situ* wear studies of surface micromachined interfaces subject to controlled loading," *Wear*, vol. 260, no. 6, pp. 580–593, Mar. 2006.
[14] D. C. Senft and M. T. Dugger, "Friction and wear in surface micromachined tribological test devices," in *Proc. SPIE—Int. Soc. Opt. Eng.*, 1997, vol. 3224, pp. 31–38.
[15] S. J. Timpe, K. Komvopoulos, and M. T. Dugger, "Microscale friction phenomena in oscillatory sliding contacts," *J. Appl. Phys.*, vol. 102, no. 12, pp. 123503-1–123503-8, Dec. 2007.
[16] D. A. Hook, S. J. Timpe, M. T. Dugger, and J. Krim, "Tribological degradation of fluorocarbon coated silicon microdevice surfaces in normal and sliding contact," *J. Appl. Phys.*, vol. 104, no. 3, pp. 034303-1–034303-6, Aug. 2008.
[17] U. Srinivasan, M. R. Houston, R. T. Howe, and R. Maboudian, "Alkyltrichlorosilane-based self-assembled monolayer films for stiction reduction in silicon micromachines," *J. Microelectromech. Syst.*, vol. 7, no. 2, pp. 252–260, Jun. 1998.
[18] W. R. Ashurst, C. Yau, C. Carraro, R. Maboudian, and M. T. Dugger, "Dichlorodimethylsilane as an anti-stiction monolayer for MEMS: A comparison to the octadecyltrichlosilane self-assembled monolayer," *J. Microelectromech. Syst.*, vol. 10, no. 1, pp. 41–49, Mar. 2001.
[19] R. Maboudian, W. R. Ashurst, and C. Carraro, "Tribological challenges in microelectromechanical systems," *Tribol. Lett.*, vol. 12, no. 2, pp. 95–100, Feb. 2002.
[20] M. P. de Boer, D. L. Luck, W. R. Ashurst, R. Maboudian, A. D. Corwin, J. A. Walraven, and J. M. Redmond, "High-performance surface-micromachined inchworm actuator," *J. Microelectromech. Syst.*, vol. 13, no. 1, pp. 63–74, Feb. 2004.
[21] D. H. Alsem, E. A. Stach, M. T. Dugger, M. Enachescu, and R. O. Ritchie, "An electron microscopy study of wear in polysilicon microelectromechanical systems in ambient air," *Thin Solid Films*, vol. 515, no. 6, pp. 3259–3266, Feb. 2007.
[22] D. H. Alsem, M. T. Dugger, E. A. Stach, and R. O. Ritchie, "Micron-scale friction and sliding wear of polycrystalline silicon thin structural films in ambient air," *J. Microelectromech. Syst.*, vol. 17, no. 5, pp. 1144–1154, Oct. 2008.
[23] W. Wang, Y. Wang, H. Bao, B. Xiong, and M. Bao, "Friction and wear properties in MEMS," *Sens. Actuators A*, vol. 97/98, pp. 486–491, Apr. 2002.
[24] J. A. Williams and H. R. Le, "Tribology and MEMS," *J. Phys. D, Appl. Phys.*, vol. 39, no. 12, pp. R201–R214, Jun. 2006.
[25] Z. Guo, Y. Meng, H. Wu, C. Su, and S. Wen, "Measurement of static and dynamic friction coefficients of sidewalls of bulk-microfabricated MEMS devices with an on-chip micro-tribotester," *Sens. Actuators A*, vol. 135, no. 2, pp. 863–869, Apr. 2007.
[26] J. Wu, S. Wang, and J. Miao, "A MEMS device for studying the friction behavior of micromachined sidewall surfaces," *J. Microelectromech. Syst.*, vol. 17, no. 4, pp. 921–933, Aug. 2008.
[27] S. T. Patton and J. S. Zabinski, "Failure mechanisms of a MEMS actuator in very high vacuum," *Tribol. Int.*, vol. 35, no. 6, pp. 373–379, Jun. 2002.
[28] S. A. Smallwood, K. C. Eapen, S. T. Patton, and J. S. Zabinski, "Performance results of MEMS coated with a conformal DLC," *Wear*, vol. 260, no. 11/12, pp. 1179–1189, Jun. 2006.
[29] K. C. Eapen, S. A. Smallwood, and J. S. Zabinski, "Lubrication of MEMS under vacuum," *Surf. Coat. Technol.*, vol. 201, no. 6, pp. 2960–2969, Dec. 2006.
[30] A. Lumbantobing and K. Komvopoulos, "Static friction in polysilicon surface micromachines," *J. Microelectromech. Syst.*, vol. 14, no. 4, pp. 651–663, Aug. 2005.
[31] S. J. Timpe and K. Komvopoulos, "An experimental study of sidewall adhesion in microelectromechanical systems," *J. Microelectromech. Syst.*, vol. 14, no. 6, pp. 1356–1363, Dec. 2005.
[32] S. J. Timpe and K. Komvopoulos, "Microdevice for measuring friction and adhesion properties of sidewall contact interfaces of microelectromechanical systems," *Rev. Sci. Instrum.*, vol. 78, no. 6, pp. 065106-1–065106-9, Jun. 2007.
[33] S. J. Timpe and K. Komvopoulos, "The effect of adhesion on the static friction properties of sidewall contact interfaces of microelectromechanical devices," *J. Microelectromech. Syst.*, vol. 15, no. 6, pp. 1612–1621, Dec. 2006.
[34] S. J. Timpe, D. H. Alsem, D. A. Hook, M. T. Dugger, and K. Komvopoulos, "Wear of polysilicon surface micromachines operated in high vacuum," *J. Microelectromech. Syst.*, vol. 18, no. 2, pp. 229–238, Apr. 2009.
[35] D. Koester, A. Cowen, R. Mahadevan, M. Stonefield, and B. Hardy, *PolyMUMPs Design Handbook, Revision 10.0*. Research Triangle Park, NC: MEMSCAP Inc., 2003.
[36] J. F. Archard, "Contact and rubbing of flat surfaces," *J. Appl. Phys.*, vol. 24, no. 8, pp. 981–988, Aug. 1953.
[37] J. F. Archard, "Single contacts and multiple encounters," *J. Appl. Phys.*, vol. 32, no. 8, pp. 1420–1425, Aug. 1961.
[38] O. N. Pierron, D. D. Macdonald, and C. L. Muhlstein, "Galvanic effects in Si-based microelectromechanical systems: Thick oxide formation and its implications for fatigue reliability," *Appl. Phys. Lett.*, vol. 86, no. 21, pp. 211919-1–211919-3, May 2005.
[39] D. H. Alsem, B. L. Boyce, E. A. Stach, and R. O. Ritchie, "Effect of post-release sidewall morphology on the fracture and fatigue properties of polycrystalline silicon structural films," *Sens. Actuators A*, vol. 147, no. 2, pp. 553–560, Oct. 2008.
[40] H. Kahn, C. Deeb, I. Chasiotis, and A. H. Heuer, "Anodic oxidation during MEMS processing of silicon and polysilicon: Native oxides can be thicker than you think," *J. Microelectromech. Syst.*, vol. 14, no. 5, pp. 914–923, Oct. 2005.

Daan Hein Alsem received the M.S. degree in applied physics from the University of Groningen, Groningen, The Netherlands, in 2002, and the Ph.D. degree in materials science and engineering from the University of California, Berkeley, in 2006.

After working as a Postdoctoral Researcher with the Materials Sciences Division and the National Center for Electron Microscopy, Lawrence Berkeley National Laboratory, Berkeley, he became the Director of Research of Hummingbird Scientific, Lacey, WA, in 2009. Since 2010, he has also been an Affiliate Assistant Professor in the Department of Mechanical Engineering, University of Washington, Seattle. His primary research interests are mechanical behavior and reliability of thin films, nanomaterials for energy applications, and novel structural materials, emphasizing the application of *in situ* electron-beam characterization of materials.

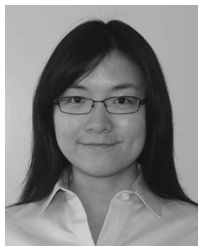

Hua Xiang received the B.S. degree in mechanical engineering and the M.S. degree in materials science and engineering from Tsinghua University, Beijing, China, in 2004 and 2007, respectively. She is currently working toward the Ph.D. degree in mechanical engineering at the University of California, Berkeley.

Her research interests are in experimental studies of the tribological properties of microelectromechanical systems.

Robert O. Ritchie received the B.A. degree in physics and metallurgy and the M.A., Ph.D., and Sc.D. degrees in materials science from the University of Cambridge, Cambridge, U.K., in 1969, 1973, 1973, and 1990, respectively.

He is currently the H.T. and Jessie Chua Distinguished Professor of Engineering in the Department of Materials Science and Engineering and the Department of Mechanical Engineering, University of California, Berkeley. He is also currently a Senior Materials Scientist with the Lawrence Berkeley National Laboratory, Berkeley. He is known for his research into the mechanics and mechanisms of fracture and fatigue of structural and biological materials, having authored over 600 papers in the technical literature. His current research interests are focused on the biological and disease-related deterioration of the structural integrity of bone and the development of damage-tolerant bulk metallic glasses and bioinspired lightweight structural materials.

Dr. Ritchie is a member of the National Academy of Engineering and the U.K. Royal Academy of Engineering.

Kyriakos Komvopoulos received the Diploma in civil engineering from the National Technical University of Athens, Athens, Greece, in 1979, and the M.S. degree in aeronautics and astronautics, the M.S. degree in civil engineering, and the Ph.D. degree in mechanical engineering from the Massachusetts Institute of Technology, Cambridge, in 1981, 1981, and 1986, respectively.

Since 1989, he has been a Professor of mechanical engineering at the University of California, Berkeley, where he is also the Founder and the Director of the Surface Sciences and Engineering Laboratory (SSEL) and the Computational Surface Mechanics Laboratory (CSML). His current research in SSEL and CSML is on surface nanoengineering, nanomaterial synthesis, analytical and finite-element method nano-/microcontact mechanics, tribology, characterization of ultrathin films deposited by RF sputtering and filtered cathodic vacuum arc, shape-memory alloys, adhesion/wear/fatigue of nano-/microelectromechanical systems, plasma surface treatments for biomedical applications, tribology and mechanics of human joints, surface chemical modification/patterning for controlling cell adhesion and proliferation, scaffolds for tissue engineering, and cell mechanics. He teaches graduate and undergraduate courses on tribology, mechanical behavior of materials, plasticity, fatigue, and fracture mechanics.

Dr. Komvopoulos is a Fellow of the American Society of Mechanical Engineers (ASME) and the Society of Tribologists and Lubrication Engineers (STLE) and a member of the American Chemical Society (ACS), American Society of Metals (ASM), and Materials Research Society (MRS). He was the recipient of several prestigious awards, including the IBM Faculty Development Award, National Science Foundation (NSF) Presidential Young Investigator Award, ASME B. L. Newkirk Award, and NSF Engineering Initiation Award.